High Partial Auxeticity Induced by Nanochannels in [111]-Direction in a Simple Model with Yukawa Interactions

Konstantin V. Tretiakov [1],*[ID]**, Paweł M. Pigłowski** [1][ID]**, Jakub W. Narojczyk** [1][ID]**, Mikołaj Bilski** [2],*[ID] **and Krzysztof W. Wojciechowski** [1][ID]

[1] Institute of Molecular Physics, Polish Academy of Sciences, Smoluchowskiego 17/19, 60-179 Poznan, Poland; pmp@ifmpan.poznan.pl (P.M.P.); narojczyk@ifmpan.poznan.pl (J.W.N.); kww@ifmpan.poznan.pl (K.W.W.)

[2] Institute of Applied Mechanics, Poznań University of Technology, Jana Pawła II 24, 60–965 Poznań, Poland

* Correspondence: tretiakov@ifmpan.poznan.pl (K.V.T.); mikolaj.bilski@put.poznan.pl (M.B.);
  Tel.: +48-61-689-52-76 (K.V.T.)

check for updates

Abstract: Computer simulations using Monte Carlo method in the isobaric-isothermal ensemble were used to investigate the impact of nanoinclusions in the form of very narrow channels in the [111]-direction on elastic properties of crystals, whose particles interact via Yukawa potential. The studies were performed for several selected values of Debye screening length ($(\kappa\sigma)^{-1}$). It has been observed that introduction of the nanoinclusions into the system reduces the negative value of Poisson's ratio towards $[110][1\bar{1}0]$, maintaining practically constant values of Poisson's ratio in the directions [100] and [111]. These studies also show that concentration of particles forming the nanoinclusions in the system has a significant effect on the value of Poisson's ratio in the $[110][1\bar{1}0]$-direction. A strong (more than fourfold) decrease of Poisson's ratio in this direction was observed, from $-0.147(3)$ (system without inclusions) to $-0.614(14)$ (system with nanoinclusions) at $\kappa\sigma = 10$ when the inclusion particles constituted about 10 percent of all particles. The research also showed an increase in the degree of auxeticity in the system with increasing concentration of nanoinclusion particles for all the screening lengths considered.

Keywords: auxetics; negative Poisson's ratio; nanochannel; colloidal crystal; model of nanocomposite

1. Introduction

Composite materials are increasingly popular in today's world mainly because of their various physical, mechanical and other properties, which are desirable in different applications [1]. Their unusual properties are used in electronics [2], in constructing the brakes of aircraft [3], or even as catalysts and adsorbents [4]. Recently, one can observe increase of interest in auxetic composites [5,6] and auxetic structures [7,8]. Auxetics, i.e., materials with negative Poisson's ratio [9–14], exhibit an unusual mechanical property: they shrink transversally under compression and increase their transverse dimensions when stretched. This property encourages one to use these materials in various devices, e.g., molecular sieves, sensors, and other applications [15]. This makes them a subject of research in the context of looking for new auxetic materials and mechanisms leading to auxeticity at various scales—both microscopic [16–22] and macroscopic [23–40]. Recently, thin films of thickness in nanometer scale have been presented that exhibit zero Poisson's ratio [41] and polymer nanocomposite foams that find applications for chemical sensors [42], electromagnetic shielding [43] or damping applications [44]. One of interesting ideas of looking for new auxetic materials is searching for auxetic composites at nano level, in particular molecular nanocomposites. This idea has been

tested recently on models of colloidal crystals using computer simulations [45,46]. A reason for such studies was presented by Demirörs et al [47] who illustrated the possibility of producing single- and multicomponent colloidal arrays in complex three-dimensional structures. In this context, good systems to create models of nanocomposites are charge-stabilized colloidal crystals [48–54], in which particles interact through the hard-core repulsive Yukawa pair potential [48–50,52] and hard-sphere potential [55]. In such models, the hard-core repulsive Yukawa pair potential describes interactions between charged colloidal particles and interaction between nonionic colloids is modeled using the hard-sphere potential. In addition, particles interacting only with the hard potential are treated as inclusions into matrices of Yukawa particles interacting via the hard-core repulsive Yukawa pair potential. Elastic properties of both the hard-sphere crystals [56] and face-centered cubic (fcc) crystals of hard-core repulsive Yukawa particles [57] are well-known. Recently, auxetic properties of systems with inclusions in the form of nanochannels or nanolayers have been studied [45,46,58,59]. This research shows that the introduction of hard inclusions into crystal of Yukawa particles induces [46] or enhances [45,58,59] auxetic properties of nanocomposite models. As both hard-sphere and Yukawa crystals are anisotropic, orientation of inclusions is expected to be relevant for elastic properties of the resulting system.

The main goal of this work was to show a strong influence of the nanoinclusions on auxetic properties of the considered model materials. In particular, we demonstrated that the introduction of nanoinclusions in the form of nanochannels in the [111]-direction into crystal of Yukawa particles leads to high partial auxeticity of the system. The latter was shown to reduce more than four times the negative value of Poisson's ratio in the $[110][1\bar{1}0]$-direction. Moreover, the reduction of Poisson's ratio in the $[110][1\bar{1}0]$-direction occurred simultaneously with almost unchanging values of Poisson's ratio in the other two main crystallographic directions, [100] and [111]. This gives a new possibility to achieve a huge enhancement of auxeticity in a selected direction.

2. Model, Method and Computation Details

2.1. The Model

We considered a system consisting of $N = N_Y + N_{HS}$ particles in periodic boundary conditions that initially form a face-centered cubic structure. The model system is shown in Figure 1. Particles N_Y, marked in figure with green, interact mutually through the hard-core repulsive Yukawa pair potential (HCRYP) [48–50,52]:

$$\beta u_{ij} = \begin{cases} \infty & , \quad r_{ij} < \sigma \\ \beta \epsilon \frac{\exp[-\kappa\sigma(r_{ij}/\sigma-1)]}{r_{ij}/\sigma}, & r_{ij} \geq \sigma. \end{cases} \tag{1}$$

where $\beta = 1/(k_B T)$, k_B is the Boltzmann constant, T is the temperature, σ is the diameter of the particle's hard core, ϵ is the contact potential, κ^{-1} is the Debye screening length and r_{ij} is the distance between the centers of i and j particles. On the other hand, the particles N_{HS} marked with red in Figure 1 represent the nanoinclusions in the form of a nanochannel in the crystallographic direction [111], which interact with each other and with the Yukawa particles via the hard sphere potential (HSP):

$$\beta u_{ij} = \begin{cases} \infty, & r_{ij} < \sigma, \\ 0, & r_{ij} \geq \sigma. \end{cases} \tag{2}$$

As a result of the introduction of a nanochannel, we have a situation in which particles in the crystal can interact with different potentials (hard or Yukawa potential), which can lead to changes in interparticle distances and in crystallographic symmetry of the studied system. In this work, we considered a system with a nanochannel oriented along [111] direction, whose particles are contained in a cylinder of a diameter $\sigma/\sqrt{3} \leq d < \sigma$. Application of periodic boundary conditions results in a system consisting of infinitely many parallel nanochannels (Figure 1c). Similar to previous

works [45,46], to analyze the impact of the nanochannels on elastic properties of the studied systems, we introduced the "concentration" parameter describing the ratio of the number of hard spheres forming the channel (N_{HS}) to all particles in the system:

$$c = \frac{N_{HS}}{N} \times 100\% \,.$$ (3)

In Table 1, concentrations of the nanoinclusion particles and parameters of the systems studied in this work are given. All symbols and signs used in the paper are explained in the text of the paper. Additional symbols useful to understand the additional notions are collected in the Supplementary Materials.
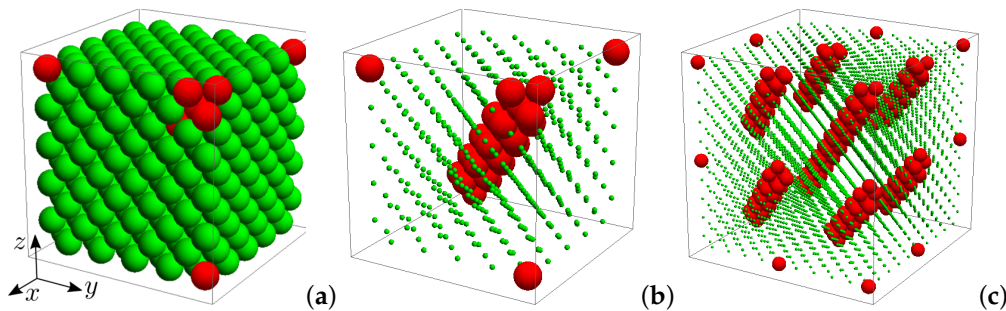

Figure 1. The structures of studied crystals with nanochannels in the [111]-crystallographic direction: (**a**) with green are marked particles which interact via the hard-core repulsive Yukawa pair potential (HCRYP), while red particles represent the hard spheres; (**b**) to better illustrate the structure of nanochannel, the centers of Yukawa particles are marked by green dots; and (**c**) periodic boundary conditions result in the structure with periodic array of nanochannels.

Table 1. Summary of the parameters of the studied systems: n, number of fcc cells on the edge of the system; N, total number of particles in the system; N_{HS}, number of hard spheres forming the inclusions; c, concentration of nanochannel particles.

n	$N = 4n^3$	$N_{HS} = 7n$	c
4	256	28	10.94%
5	500	35	7.000%
6	864	42	4.861%
7	1372	49	3.571%
8	2048	56	2.734%

2.2. Method

The studies were conducted by computer simulations using Monte Carlo (MC) method in an isobaric-isothermal (NpT) ensemble. To determine elastic properties of the studied systems, the Parrinello–Rahman method [60–63] with variable shape of the periodic box was used (details in the Supplementary Materials). According to this approach, tensor of elastic compliances S_{ijkl} can be determined directly by analyzing the fluctuations of the strain tensor:

$$S_{ijkl} = \langle \Delta\varepsilon_{ij}\Delta\varepsilon_{kl} \rangle V_p / k_B T \,,$$ (4)

where ε_{ij} are elements of the strain tensor $\Delta\varepsilon_{ij} \equiv \varepsilon_{ij} - \langle\varepsilon_{ij}\rangle$, V_p is the equilibrium volume of the system at pressure P, and

$$\varepsilon = \left(\mathbf{h}_0^{-1} \cdot \mathbf{h} \cdot \mathbf{h} \cdot \mathbf{h}_0^{-1} - \mathbf{I} \right) / 2 \,.$$ (5)

In Equation (5), $\mathbf{h}_0 \equiv \langle \mathbf{h} \rangle$ is the reference box matrix; $\mathbf{h}$ matrix, in which the columns are formed by the edges of the simulation box, represents instantaneous values of the simulation box in each

simulation step; and **I** is the identity matrix. $\langle ... \rangle$ means the average over the NpT ensemble (matrices $\mathbf{h}_0$ and $\mathbf{h}$ are kept symmetric). Knowledge of all (21 in the general case) elements of the elastic compliance tensor allows for a full description of elastic properties of the studied system and for determination of Poisson's ratio in any crystallographic direction [46,64]:

$$\nu_{nm} = -\frac{m_i m_j S_{ijkl} n_k n_l}{n_p n_r S_{prst} n_s n_t} \, , \tag{6}$$

where: n_i and m_i are the components of unit vectors $\vec{\mathbf{n}}$ and $\vec{\mathbf{m}}$, respectively. The $\vec{\mathbf{n}}$ versor represents the direction in which the external stress is applied. The $\vec{\mathbf{m}}$ versor indicates the direction in which one measures the deformation induced by applied stress (see the Supplementary Materials).

The possibility of determining Poisson's ratio in any crystallographic direction allows one to analyze the impact of the nanochannel on auxetic properties in the entire system, not only in a single specific direction. For this purpose, we calculated the coefficient, previously proposed by us [65], which determines the degree of auxeticity of the system:

$$\chi = \sqrt[3]{\frac{3A}{4\pi}} \, , \tag{7}$$

where

$$A = \int\limits_0^{2\pi} \int\limits_0^{\pi} \int\limits_0^{R(\theta,\phi)} r^2 \mathrm{d}r \sin\theta d\theta d\phi \, , \tag{8}$$

and

$$R(\theta, \phi) = \frac{1}{2\pi} \int\limits_0^{\pi} \left(\left| \nu_{n(\theta,\phi)}(\alpha) \right| - \nu_{n(\theta,\phi)}(\alpha) \right) \mathrm{d}\alpha \tag{9}$$

is the average *negative* value of Poisson's ratio towards $\vec{\mathbf{n}}$-direction, while α is the angle between the $\vec{\mathbf{m}}$-direction, in which the Poisson's ratio is measured, and the direction resulting from intersection of the OXY plane and the plane perpendicular to $\vec{\mathbf{n}}$ [45]. The derivation of χ is described and illustrated in detail in the Supplementary Materials of the work [65].

2.3. Computational Details

Based on the pre-determined phase diagrams [48,50] and on the results of elastic properties of Yukawa crystals [57] and hard spheres [56], simulations were conducted at reduced pressure $p^* \equiv \beta P \sigma^3 = 100$ for contact potential values $\beta\epsilon = 20$ and three Debye screening lengths $(\kappa\sigma)^{-1}$. The length of a single simulation run was 2×10^6 MC cycles after equilibration (the MC cycle contains a trial step performed for each particle, which results in N single particle trial steps, and integer part of the square root of N trail steps in which the periodic box matrix is changed (see, e.g., [63])). Simulations for each of the phase points studied were performed for at least 10 independent structures, for which the average values of elastic compliances were determined.

The intermolecular potential (Equation (1)) was truncated at a distance $r_{\text{cut}} = 2.5\sigma$. Therefore, long-range corrections were considered during calculations of potential energy of the system. The choice of $r_{\text{cut}} = 2.5\sigma$ resulted from the fact that intermolecular potentials for parameters considered in this work are short-ranged [65]. The correctness of selection of the value r_{cut} was verified by calculating Poisson's ratio in the auxetic direction ($[110][1\bar{1}0]$) with respect to r_{cut}. It was found that the results obtained for $r_{\text{cut}} = 2.5\sigma$ are in very good agreement with results obtained for larger distances of potential truncation [65].

3. Results and Discussion

3.1. Elastic Compliances and Symmetry of the System

As mentioned above, initial structure of the system was the fcc structure. Introduction of nanoinclusions into the system changed its structure, which during the simulation was manifested by the change of the form of the box matrix. As shown in Figure 2, the equilibrium form of the box matrix was achieved after about 10^3 MC cycles. The matrix is symmetrical and describes the shape of the rhombohedron:

$$\langle \mathbf{h} \rangle = \begin{bmatrix} \langle h_{xx} \rangle & \langle h_{xy} \rangle & \langle h_{xy} \rangle \\ \cdot & \langle h_{xx} \rangle & \langle h_{xy} \rangle \\ \cdot & \cdot & \langle h_{xx} \rangle \end{bmatrix} . \tag{10}$$

As a result of the simulations performed, using Equations (4) and (5), elastic compliance tensor **S** was determined, which using the Voigt (matrix) notation can be written in the following form:

$$\begin{bmatrix} S_{11} & S_{12} & S_{12} & S_{14} & S_{15} & S_{15} \\ \cdot & S_{11} & S_{12} & S_{15} & S_{14} & S_{15} \\ \cdot & \cdot & S_{11} & S_{15} & S_{15} & S_{14} \\ \cdot & \cdot & \cdot & S_{44} & S_{45} & S_{45} \\ \cdot & \cdot & \cdot & \cdot & S_{44} & S_{45} \\ \cdot & \cdot & \cdot & \cdot & \cdot & S_{44} \end{bmatrix} . \tag{11}$$

To simplify the form of the compliance tensor, the coordinate system was rotated in such a way that the [111]-direction became the [001]-direction. In the new coordinate system, the compliance tensor reads $S'_{ijkl} = R_{ip} R_{jr} R_{ks} R_{lt} S_{prst}$, where R_{ij} represents the components of the rotation matrix in the form:

$$\mathbf{R} = \frac{1}{\sqrt{6}} \begin{bmatrix} -\sqrt{3} & \sqrt{3} & 0 \\ -1 & -1 & 2 \\ \sqrt{2} & \sqrt{2} & \sqrt{2} \end{bmatrix} . \tag{12}$$
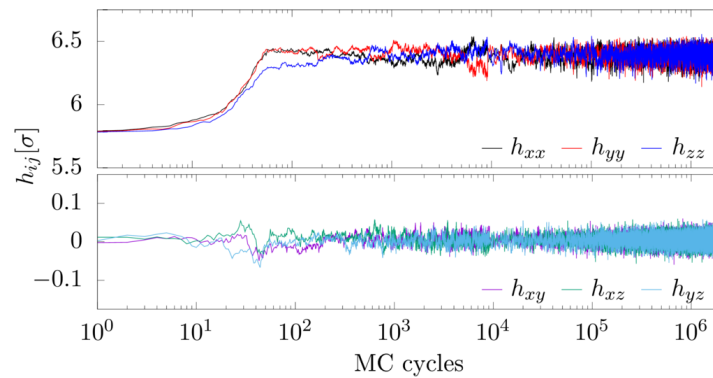

Figure 2. Components of the simulation box of the system versus MC cycles, studied at: $N = 256$, $c = 10.94\%$, $p^* = 100$, $\kappa\sigma = 10$ and $\beta\epsilon = 20$.

Finally, the S'_{ijkl} tensor can be written as a matrix $S'_{\alpha\beta}$ using the Voigt notation [66]:

$$\mathbf{S'} = \begin{bmatrix} S'_{11} & S'_{12} & S'_{13} & S'_{14} & 0 & 0 \\ \cdot & S'_{11} & S'_{13} & -S'_{14} & 0 & 0 \\ \cdot & \cdot & S'_{33} & 0 & 0 & 0 \\ \cdot & \cdot & \cdot & S'_{44} & 0 & 0 \\ \cdot & \cdot & \cdot & \cdot & S'_{44} & 2S'_{14} \\ \cdot & \cdot & \cdot & \cdot & \cdot & 2(S'_{11} - S'_{12}) \end{bmatrix} . \tag{13}$$

Relations between the matrix elements in Equations (11) and (13) are as follows:

$$S'_{11} = \frac{1}{4}(2S_{11} + 2S_{12} - 4S_{15} + S_{44}),$$

$$S'_{33} = \frac{1}{3}(S_{11} + 2S_{12} + 2S_{14} + 4S_{15} + S_{44} + 2S_{45}),$$

$$S'_{12} = \frac{1}{12}(2S_{11} + 10S_{12} - 8S_{14} - 4S_{15} - S_{44} + 4S_{45}),$$

$$S'_{13} = \frac{1}{6}(2S_{11} + 4S_{12} + S_{14} + 2S_{15} - S_{44} - 2S_{45}),$$

$$S'_{44} = \frac{1}{3}(4S_{11} - 4S_{12} - 4S_{14} + 4S_{15} + S_{44} - S_{45}),$$

$$S'_{14} = \frac{1}{3\sqrt{2}}(-2S_{11} + 2S_{12} - S_{14} + S_{15} + S_{44} - S_{45}).$$

The form of the elastic compliance matrix in Equation (13) indicates that the system has a trigonal symmetry [66]. Thus, the presence of the nanoinclusions in the form of a channel in the [111]-crystallographic direction resulted in a change of the crystallographic structure from the fcc to trigonal. Increasing concentration of particles forming the nanoinclusion had a strong impact on elastic properties of the studied system, as shown in Figure 3. The values of S_{11} and S_{12} changed significantly with the increase of c; an increase of S_{11} and a decrease of S_{12} were observed. In addition, elements S_{14}, S_{15} and S_{45} became non-zero, with component S_{45} taking negative values, very close to 0. These changes have a significant impact on Poisson's ratio.
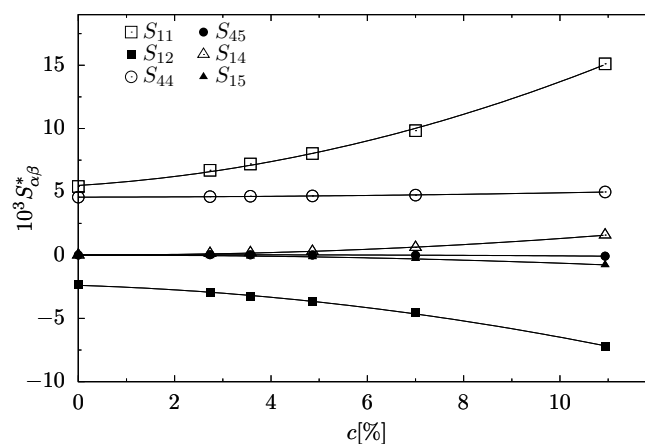

Figure 3. Elements of the elastic compliance matrix **S** with respect to the concentration, studied at: $p^* = 100$, $\kappa\sigma = 10$ and $\beta\epsilon = 20$.

3.2. Size Effects

Influence of the number of supercells and the shape of the simulated periodic box on Poisson's ratio was analyzed (see Figure 4). A weak dependence of Poisson's ratio with respect to the number and distribution of the supercells in the periodic box was observed, similar to previous studies [45] regarding the model with channel towards [001]. Thus, in this paper, the simulation results are presented for systems represented by single elementary supercells, whose parameters are given in Table 1.

In Figure 4, it is worth noting the small changes of Poisson's ratio in the crystallographic directions [100] and [111], which were related to the presence of the nanoinclusions. On the other hand, in the [110]-direction, large changes of Poisson's ratio in comparison to the system without the nanoinclusions were observed.
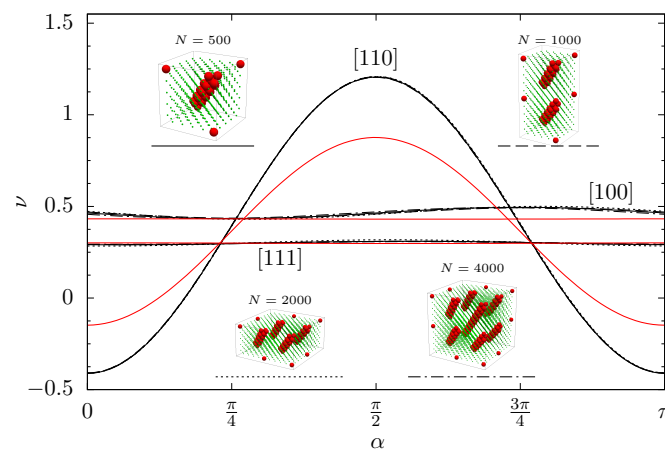
Figure 4. Poisson's ratio in three crystallographic directions for various size of the system ($N = 500$, 1000, 2000, and 4000) as a function of the angle α (with $c = 7\%$, $p^* = 100$, $\kappa\sigma = 10$ and $\beta\epsilon = 20$). Red lines represent Poisson's ratio in the respective crystallographic directions of the system without nanoinclusions.

3.3. Poisson's Ratio

In general, Poisson's ratio is influenced by both the concentration of particles forming the inclusion (c) and the value of the screening length of the potential ($(\kappa\sigma)^{-1}$). In Figure 5, Poisson's ratios in the main crystallographic directions are plotted for studied values of screening length, with respect to the concentration. Figure 5a,b shows a rather weak influence of presence of the nanoinclusions on Poisson's ratio in the directions [100] and [111], as well as its poor dependence on the screening length—which is consistent with previous studies [57]. In the direction $[110][1\bar{1}0]$ (Figure 5c), for each screening length studied, the increase in concentration caused Poisson's ratio to decrease in direction $[110][1\bar{1}0]$, i.e., enhancing auxetic properties. The lowest value of Poisson's ratio observed in these studies equals $\nu_{\min} = -0.614(14)$ and was measured in the $[110][1\bar{1}0]$-direction for concentration $c = 10.9375\%$, $\kappa\sigma = 10$ and $\beta\epsilon = 20$. The analysis of these dependencies in the main crystallographic directions suggests the possibility of selective strengthening of auxetic properties of the system. Namely, one can lower Poisson's ratio for larger concentrations of particles of nanoinclusions in one of the main crystallographic directions ($[110][1\bar{1}0]$), while, in the crystallographic directions [100] and [111], the value of Poisson's ratio remains almost constant (Figure 5).

On the other hand, the minimum values of Poisson's ratio determined in all the auxetic crystallographic directions (Figure 6) strongly decreased with the increase of concentration of particles forming nanoinclusions. This observation indicates the enhancement of auxetic properties in the whole system for higher values of concentration of particles of nanoinclusions.
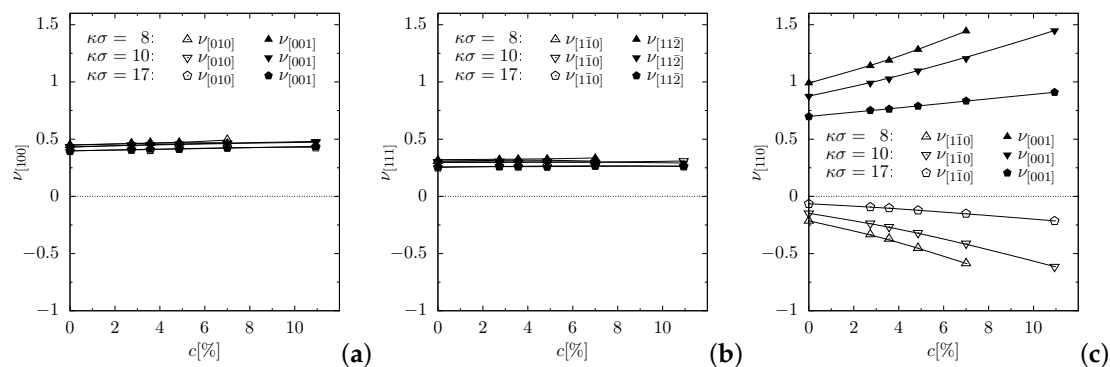

Figure 5. Poisson's ratio of Yukawa crystals with nanochannels in the main crystallographic directions with respect to the concentration: (**a**) [100]; (**b**) [111]; and (**c**) [110].
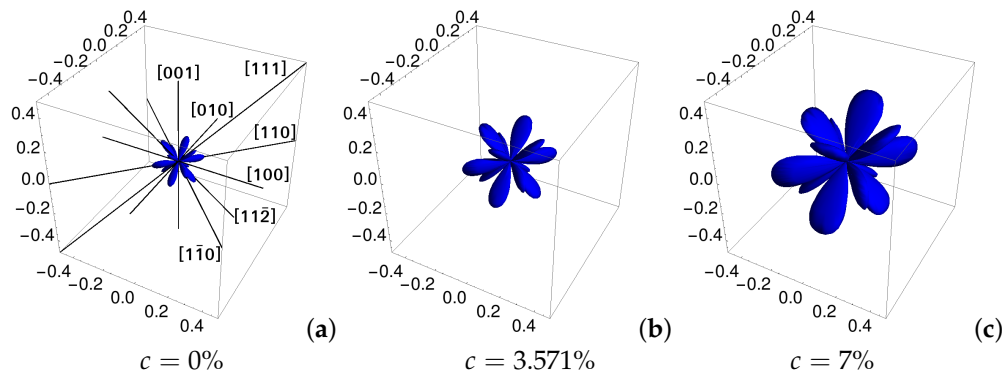
Figure 6. Absolute value of the minimal negative Poisson's ratio in all crystallographic directions for Yukawa systems with nanochannels in the [111]-direction for inverse screening length $\kappa\sigma = 10$ and various concentrations: (**a**) $c = 0\%$; (**b**) $c = 3.571\%$; and (**c**) $c = 7\%$.

3.4. The Degree of Auxeticity

To determine the influence of nanoinclusions on the auxetic properties of the system, dependence of the degree of auxeticity χ (Equation (7)) with respect to the concentration of nanoinclusion particles was determined (Figure 7). The inserts in Figure 7 show the surface of the average negative values of Poisson's ratio (Equation (9)) in all crystallographic directions for $\kappa\sigma = 10$. The increase of volume of the drawings clearly signifies the strengthening of auxetic properties and translates directly into the growth of χ with concentration. The resulting value of $\chi = 0.061$ is one of the largest of all Yukawa systems with structural modifications studied thus far [45,46,58,65]. Analysis of the results obtained indicates a significant increase of the degree of auxeticity of the whole system: 4.5 times for $\kappa\sigma = 8$, 7.5 times for $\kappa\sigma = 10$ and almost 7 times for $\kappa\sigma = 17$. Based on these observations, we can postulate a high partial auxeticity in crystals with Yukawa interactions induced by nanoinclusions in the form of nanochannels in the [111]-direction.
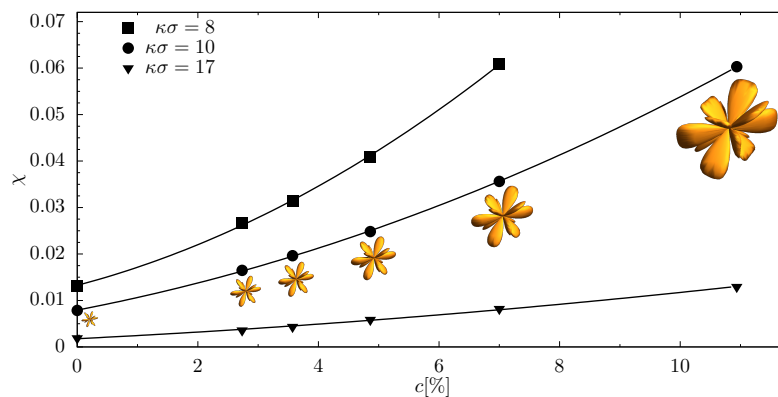

Figure 7. Degree of auxeticity with respect to the concentration for various values of screening length. The inserts in the figure show the average absolute value of negative Poisson's ratio (Equation (9)) in all crystallographic directions for $\kappa\sigma = 10$. The surface consists of the points that represent $R(\theta, \phi)$. All the inserted figures are presented at the same scale.

4. Conclusions

Using the Monte Carlo method, computer simulations of model crystals, in which particles interact with each other by Yukawa potential and the particles constituting the inclusions interact with all other particles by hard potential, were performed. The simulations showed that introduction of inclusions into the model system in the form of nanochannels in the crystallographic direction [111] causes a change of its crystal structure from the fcc to a trigonal one. Elastic properties of model crystals with various concentrations of nanoinclusion particles were determined for several values

of Debye screening length. These calculations showed a significant reduction of Poisson's ratio in the $[110][1\bar{1}0]$-direction with increasing concentration of particles forming the channels. The value of Poisson's ratio in this direction decreased more than four times from $-0.147(3)$ to $-0.614(14)$. A separate consideration was given to the fact that the presence of nanoinclusions in a system, which reduced the negative value of Poisson's ratio in the $[110][1\bar{1}0]$-direction, almost did not affect values of Poisson's ratio in the other two main crystallographic directions, $[100]$ and $[111]$. In these directions, Poisson's ratio has values close to those in the system without inclusions. It is worth noting that this effect was observed for all studied values of the Debye screening length.

Finally, one should stress that the model crystals with nanoinclusions in the form of channels in the crystallographic direction $[111]$ show the highest degree of auxeticity among all systems of this type studied thus far. It was observed that the presence of nanoinclusions results in a significant increase of the degree of auxeticity of the whole system: 4.5 times for $\kappa\sigma = 8$, 7.5 times for $\kappa\sigma = 10$ and almost 7 times for $\kappa\sigma = 17$.

One should realize that the model under consideration is based on certain simplifications and assumptions, inter alia related to the interaction potentials of colloidal particles and the possibility of modifying crystalline structure. However, we believe that the rapid development of nanotechnology (in particular, the work by Demirörs et al. [47]) brings us closer to obtaining real systems similar to the models presented in this paper. Then, one can speculate that materials based on the considered model could be used, e.g., as sensors or damping applications for vibration control in a given direction. Besides, the results obtained in this work have a general character and can be helpful in construction of materials with given elastic properties and not only in the nanoscale. Undoubtedly, an important aspect of this research is also the indication of the direction of research on the synthesis of auxetic nanocomposites.

Abbreviations

The following abbreviations are used in this manuscript:

MC	Monte Carlo
HS	Hard Sphere
HCRYP	Hard-Core Repulsive Yukawa Potential

References

1. Jones, R.M. *Mechanics of Composite Materials*, 2nd ed.; Francis & Taylor: Philadelphia, PA, USA, 1999.
2. Stankovich, S.; Dikin, D.A.; Dommett, G.H.; Kohlhaas, K.M.; Zimney, E.J.; Stach, E.A.; Piner, R.D.; Nguyen, S.T.; Ruoff, R.S. Graphene-based composite materials. *Nature* **2006**, *442*, 282–286. [CrossRef] [PubMed]
3. Rao, J.G.; Sinnur, K.H.; Jain, R.K. Effect of weave texture of carbon fabric on mechanical, thermal and tribological properties of carbon/carbon aircraft brakes. *Int. J. Compos. Mater.* **2015**, *5*, 89–96. [CrossRef]

4. Davis, M.E. Ordered porous materials for emerging applications. *Nature* **2002**, *417*, 813–821. [CrossRef]

5. Alderson, K.L.; Simkins, V.R.; Coenen, V.L.; Davies, P.J.; Alderson, A.; Evans, K.E. How to make auxetic fibre reinforced composites. *Phys. Status Solidi B-Basic Solid State Phys.* **2005**, *242*, 509–518. [CrossRef]

6. Xianglong, Y.; Ji, Z.; Haiyi, L.; Zhengyi, J.; Lingling, W. Mechanical metamaterials associated with stiffness, rigidity and compressibility: A brief review. *Prog. Mater. Sci.* **2018**, *94*, 114–173.

7. Lim, T.C. Analogies across auxetic models based on deformation mechanism. *Phys. Status Solidi Rapid Res. Lett.* **2017**, *11*, 1600440. [CrossRef]

8. Ren, X.; Das, R.; Tran, J.P.; Ngo, T. Auxetic metamaterials and structures: A review. *Smart Mater. Struct.* **2018**, *27*, 023001. [CrossRef]

9. Lakes, R.S. Foam structures with a negative Poisson's ratio. *Science* **1987**, *235*, 1038–1040. [CrossRef]

10. Wojciechowski, K.W. Two-dimensional isotropic model with a negative Poisson ratio. *Phys. Lett. A* **1989**, *137*, 60–64. [CrossRef]

11. Evans, K.E.; Nkansah, M.A.; Hutchinson, I.J.; Rogers, S.C. Molecular network design. *Nature* **1991**, *353*, 124. [CrossRef]

12. Baughman, R.H. Avoiding the shrink. *Nature* **2003**, *425*, 667. [CrossRef] [PubMed]

13. Greaves, G.N.; Greer, A.L.; Lakes, R.S.; Rouxel, T. Poisson's ratio and modern materials. *Nat. Mater.* **2011**, *10*, 823–837. [CrossRef]

14. Lim, T.C. *Auxetic Materials and Structures*; Springer: Singapore, 2015. [CrossRef]

15. Duncan, O.; Shepherd, T.; Moroney, C. Review of auxetic materials for sports applications: Expanding options in comfort and protection. *Appl. Sci. Basel* **2018**, *8*, 941. [CrossRef]

16. Wang, Y.; Ding, Y. Mechanical and electronic properties of stoichiometric silicene and germanene oxides from first-principles. *Phys. Status Solidi Rapid Res. Lett.* **2013**, *7*, 410–413. [CrossRef]

17. Ho, D.T.; Kim, H.; Kwon, S.Y.; Kim, S.Y. Auxeticity of face–centered cubic metal (001) nanoplates. *Phys. Status Solidi B-Basic Solid State Phys.* **2015**, *252*, 1492–1501. [CrossRef]

18. Azzopardi, K.M.; Brincat, J.P.; Grima, J.N.; Gatt, R. Advances in the study of the deformation mechanism of stishovite. *Phys. Status Solidi B-Basic Solid State Phys.* **2015**, *252*, 1486–1491. [CrossRef]

19. Baimova, J.A.; Rysaeva, L.K.; Liu, B.; Dmitriev, S.V.; Zhou, K. From flat graphene to bulk carbon nanostructures. *Phys. Status Solidi B-Basic Solid State Phys.* **2015**, *252*, 1502–1507. [CrossRef]

20. Grima, J.N.; Zerafa, C.; Brincat, J.P. Development of novel poly(phenylacetylene) network polymers and their mechanical behaviour. *Phys. Status Solidi B-Basic Solid State Phys.* **2014**, *251*, 375–382. [CrossRef]

21. Grima, J.N.; Zerafa, C. On the effect of solvent molecules on the structure and mechanical properties of organic polyphenylacetylene auxetic re–entrant network polymers. *Phys. Status Solidi B-Basic Solid State Phys.* **2013**, *250*, 2030–2037. [CrossRef]

22. Ho, D.T.; Park, S.; Kwon, S.; Han, T.; Kim, S.Y. Negative Poisson's ratio in cubic materials along principal directions. *Phys. Status Solidi B-Basic Solid State Phys.* **2016**, *253*, 1288–1294. [CrossRef]

23. Kolpakov, A.G. Determination of the average characteristics of elastic frameworks. *J. Appl. Math. Mech.* **1985**, *49*, 739–745. [CrossRef]

24. Gibson, L.J.; Ashby M.F. *Cellular Solids, Structure and Properties*; Cambridge University Press: Cambridge, UK, 1997.

25. Mizzi, L.; Azzopardi, K.M.; Attard, D.; Grima, J.N.; Gatt, R. Auxetic metamaterials exhibiting giant negative Poisson's ratios. *Phys. Status Solidi Rapid Res. Lett.* **2015**, *9*, 425–430. [CrossRef]

26. Jensen, A.W.; Zhao, H.; Norbury, A.; Li, L.; Rothwell, G.; Ren, J. Effects of Poisson's ratio on the deformation of thin membrane structures under indentation. *Phys. Status Solidi B-Basic Solid State Phys.* **2015**, *252*, 1526–1532. [CrossRef]

27. Slann, A.; White, W.; Scarpa, F.; Boba, K.; Farrow, I. Cellular plates with auxetic rectangular perforations. *Phys. Status Solidi B-Basic Solid State Phys.* **2015**, *252*, 1533–1539. [CrossRef]

28. Strek, T.; Jopek, H.; Nienartowicz, M. Dynamic response of sandwich panels with auxetic cores. *Phys. Status Solidi B-Basic Solid State Phys.* **2015**, *252*, 1540–1550. [CrossRef]

29. Jopek, H.; Strek, T. Thermal and structural dependence of auxetic properties of composite materials. *Phys. Status Solidi B-Basic Solid State Phys.* **2015**, *252*, 1551–1558. [CrossRef]

30. Mizzi, L.; Gatt, R.; Grima, J.N. Non-porous grooved single-material auxetics. *Phys. Status Solidi B-Basic Solid State Phys.* **2015**, *252*, 1559–1564. [CrossRef]

31. Hoover, W.G.; Hoover, C.G. Searching for auxetics with DYNA3D and ParaDyn. *Phys. Status Solidi B-Basic Solid State Phys.* **2005**, *242*, 585–594. [CrossRef]

32. Gatt, R.; Caruana-Gauci, R.; Attard, D.; Casha, A.R.; Wolak, W.; Dudek, K.; Mizzi, L.; Grima, J.N. On the properties of real finite-sized planar and tubular stent-like auxetic structures. *Phys. Status Solidi B-Basic Solid State Phys.* **2014**, *251*, 321–327. [CrossRef]

33. Mizzi, L.; Attard, D.; Casha, A.; Grima, J.N.; Gatt, R. On the suitability of hexagonal honeycombs as stent geometries. *Phys. Status Solidi B-Basic Solid State Phys.* **2014**, *251*, 328–337. [CrossRef]

34. Rodriguez, B.; Kalathur, H.; Lakes, R. A sensitive piezoelectric composite lattice: Experiment. *Phys. Status Solidi B-Basic Solid State Phys.* **2014**, *251*, 349–353. [CrossRef]

35. Strek, T.; Jopek, H.; Maruszewski, B.T.; Nienartowicz, M. Computational analysis of sandwich-structured composites with an auxetic phase. *Phys. Status Solidi B-Basic Solid State Phys.* **2014**, *251*, 354–366. [CrossRef]

36. Airoldi, A.; Bettini, P.; Panichelli, P.; Oktem, M.F.; Sala, G. Chiral topologies for composite morphing structures? Part I: Development of a chiral rib for deformable airfoils. *Phys. Status Solidi B-Basic Solid State Phys.* **2015**, *252*, 1435–1445. [CrossRef]

37. Wang, Y.C.; Shen, M.W.; Liao, S.M. Microstructural effects on the Poisson's ratio of star-shaped two-dimensional systems. *Phys. Status Solidi B-Basic Solid State Phys.* **2017**, *254*, 1700024. [CrossRef]

38. Cauchi, R.; Attard, D.; Grima, J.N. On the mechanical properties of centro–symmetric honeycombs with T–shaped joints. *Phys. Status Solidi B-Basic Solid State Phys.* **2013**, *250*, 2002–2011. [CrossRef]

39. Gatt, R.; Attard, D.; Farrugia, P.S.; Azzopardi, K.M.; Mizzi, L.; Brincat, J.P.; Grima, J.N. A realistic generic model for anti–tetrachiral systems. *Phys. Status Solidi B-Basic Solid State Phys.* **2013**, *250*, 2012–2019. [CrossRef]

40. Khakalo, S.; Balobanov, V.; Niiranen, J. Modelling size-dependent bending, buckling and vibrations of 2D triangular lattices by strain gradient elasticity models: Applications to sandwich beams and auxetics. *Int. J. Eng. Sci.* **2018**, *127*, 33–52. [CrossRef]

41. Nguyen, C.; Maheshwari, V.; Saraf, R.F. Ultrasoft 100 nm Thick Zero Poisson's Ratio Film with 60% Reversible Compressibility. *Nano Lett.* **2012**, *12*, 2171. [CrossRef]

42. Wang, Y.B.; Sotzing, G.A.; Weiss, R.A. Porous composites coated with hybrid nano carbon materials perform excellent electromagnetic interference shielding. *Chem. Mater.* **2003**, *15*, 375. [CrossRef]

43. Chen, Y.J.; Li, Y.; Chu, B.T.T.; Kuo, I.T.; Yip, M.C.; Tai, N. Porous composites coated with hybrid nano carbon materials perform excellent electromagnetic interference shielding. *Compos. Part B* **2015**, *70*, 231. [CrossRef]

44. Zhang, X.C.; Scarpa, F.; McHale, R.; Limmack, A.P.; Peng, H.X. Carbon nano-ink coated open cell polyurethane foam with micro-architectured multilayer skeleton for damping applications. *RSC Adv.* **2016**, *6*, 80334. [CrossRef]

45. Tretiakov, K.V.; Piglowski, P.M.; Hyzorek, K.; Wojciechowski, K.W. Enhanced auxeticity in Yukawa systems due to introduction of nanochannels in [001]-direction. *Smart Mater. Struct.* **2016**, *25*, 054007. [CrossRef]

46. Piglowski, P.M.; Wojciechowski, K.W.; Tretiakov, K.V. Partial auxeticity induced by nanoslits in the Yukawa crystal. *Phys. Status Solidi-Rapid Res. Lett.* **2016**, *10*, 566–569. [CrossRef]

47. Demirors, A.F.; Pillai, P.P.; Kowalczyk, B.; Grzybowski, B.A. Colloidal assembly directed by virtual magnetic moulds. *Nature* **2013**, *503*, 99–103. [CrossRef] [PubMed]

48. Azhar, F.E.; Baus, M.; Ryckaert, J.P. Line of triple points for the hard-core Yukawa model: A computer simulation study. *J. Chem. Phys.* **2000**, *112*, 5121–5126. [CrossRef]

49. Auer, S.; Frenkel, D. Crystallization of weakly charged colloidal spheres: a numerical study. *J. Phys.-Condes. Matter* **2002**, *14*, 7667–7680. [CrossRef]

50. Hynninen, A.P.; Dijkstra, M. Phase diagrams of hard-core repulsive Yukawa particles. *Phys. Rev. E* **2003**, *68*, 021407. [CrossRef] [PubMed]

51. Hansen, J.P.; McDonald, I.R. *Theory of Simple Liquids*; Academic Press: Amsterdam, The Netherlands, 2006.

52. Colombo, J.; Dijkstra, M. Effect of quenched size polydispersity on the fluid-solid transition in charged colloidal suspensions. *J. Chem. Phys.* **2011**, *134*, 154504. [CrossRef]

53. Heinen, M.; Holmqvist, P.; Banchio, A.J.; Nagele, G. Pair structure of the hard-sphere Yukawa fluid: An improved analytic method versus simulations, Rogers-Young scheme, and experiment. *J. Chem. Phys.* **2011**, *134*, 044532. [CrossRef]

54. Van der Linden, M.N.; van Blaaderen, A.; Dijkstra, M. Effect of size polydispersity on the crystal-fluid and crystal-glass transition in hard-core repulsive Yukawa systems. *J. Chem. Phys.* **2013**, *138*, 114903. [CrossRef]

55. Alder, B.J.; Wainwright, T.E. Phase Transition for a Hard Sphere System. *J. Chem. Phys.* **1957**, *27*, 1208–1209. [CrossRef]

56. Tretiakov, K.V.; Wojciechowski, K.W. Poisson's ratio of the fcc hard sphere crystal at high densities. *J. Chem. Phys.* **2005**, *123*, 074509. [CrossRef] [PubMed]

57. Tretiakov, K.V.; Wojciechowski, K.W. Partially auxetic behavior in fcc crystals of hard-core repulsive Yukawa particles. *Phys. Status Solidi B-Basic Solid State Phys.* **2014**, *251*, 383–387. [CrossRef]

58. Piglowski, P.M.; Narojczyk, J.W.; Poźniak, A.A.; Wojciechowski, K.W.; Tretiakov, K.V. Auxeticity of Yukawa systems with nanolayers in the (111) crystallographic plane. *Materials* **2017**, *10*, 1338. [CrossRef] [PubMed]

59. Tretiakov, K.V.; Piglowski, P.M.; Narojczyk, J.W.; Wojciechowski, K.W. Selective enhancement of auxeticity through changing a diameter of nanochannels in Yukawa systems. *Smart Mater. Struct.* **2018**, *27*, 115021. [CrossRef]

60. Parrinello, M.; Rahman, A. Polymorphic transitions in single crystals: A new molecular dynamics method. *J. Appl. Phys.* **1981**, *52*, 7182–7190. [CrossRef]

61. Parrinello, M.; Rahman, A. Strain fluctuations and elastic constants. *J. Chem. Phys.* **1982**, *76*, 2662–2666. [CrossRef]

62. Wojciechowski, K.W.; Branka, A.C.; Parrinello, M. Monte Carlo study of the phase diagram of a two dimensional system of hard cyclic hexamers. *Mol. Phys.* **1984**, *53*, 1541–1545. [CrossRef]

63. Wojciechowski, K.W.; Tretiakov, K.V.; Kowalik, M. Elastic properties of dense solid phases of hard cyclic pentamers and heptamers in two dimensions. *Phys. Rev. E* **2003**, *67*, 036121. [CrossRef] [PubMed]

64. Tokmakova, S.P. Stereographic projections of Poisson's ratio in auxetic crystals. *Phys. Status Solidi B-Basic Solid State Phys.* **2005**, *242*, 721–729. [CrossRef]

65. Piglowski, P.M.; Narojczyk, J.W.; Wojciechowski, K.W.; Tretiakov, K.V. Auxeticity enhancement due to size polydispersity in fcc crystals of hard-core repulsive Yukawa particles. *Soft Matter* **2017**, *13*, 7916–7921. [CrossRef]

66. Nye, J.F. *Physical Properties of Crystalls, Their Representation by Tensors and Matrices*; Clarendon Press: Oxford, UK, 1957.